Thus, a rapid rate of change alone does not explain why change at the set of positively selected codons appears to be adaptive.

Conclusion

We have identified a small set of rapidly evolving codons in the HA1 domain of the hemagglutinin gene of human influenza A subtype H3 in which replacement substitutions in the past appear to have been selectively advantageous. Strains with more mutations in these codons were more likely to be the progenitors of successful new lineages in 9 of 11 influenza seasons. The probability of obtaining a successful test by chance varied across years. However, our method produced successful tests in many years, such as 1993–1994, when it was highly unlikely to do so. A causal explanation for our results is suggested by the significant overlap between the positively selected codons and the codons in or near antibody combining sites A or B and, to a lesser extent, codons associated with the sialic acid receptor binding site. However, codons associated with these sites of known function that are not under positive selection perform poorly in the prediction tests. The positively selected codons are among the most quickly evolving in the HA1 domain of hemagglutinin, but this characteristic also is not a sufficient explanation for our results. It appears that we have identified a subset of rapidly evolving codons in known functional sites for which change in the past has been associated with a clear selective advantage. Whether additional changes in these codons will confer a selective advantage in the future remains to be seen. Our retrospective tests indicate that, had these data been available in the past, monitoring change in the positively selected codons might have provided potentially useful information about the course of influenza evolution. These methods can be used to examine the evolution of the hemagglutinins of influenza B and influenza A H1 viruses circulating in humans to identify sets of positively selected codons that may have predictive value for these important pathogens.

References and Notes

1. W. M. Fitch, R. M. Bush, C. A. Bender, N. J. Cox, *Proc. Natl. Acad. Sci. U.S.A.* **94**, 7712 (1997).
2. R. M. Bush, W. M. Fitch, C. A. Bender, N. J. Cox, *Mol. Biol. Evol.* **16**, 1457 (1999).
3. The technique for identifying those codons under positive selection excludes amino acid replacements that may have occurred during culture in eggs in the laboratory by ignoring replacements that occur on the branches joining isolate sequences to the tree.
4. Sequences were generated at the Centers for Disease Control and Prevention by the protocols described in (*1*). They have been deposited in GenBank (accession nos. AF008656 to AF008909 and AF180564 to AF180666).
5. D. L. Swofford, PAUP* (Phylogenetic Analysis Using Parsimony and other methods) version 4.0.0d60.
6. We used trees constructed from the 1983–1997 data both to derive the set of positively selected codons (*2*) and to score the prediction tests. This does not bias our scoring because the location of the trunk is not a factor in determining which codons are under positive selection.
7. Trunk nodes present in at least 50% of the bootstrap replicates were consistently present in nucleotide parsimony and neighbor-joining trees and also in trees constructed from amino acids using either parsimony, neighbor-joining (*5*), or the protML maximum likelihood routine of Molphy 2.2 (made available by J. Adachi and M. Hasegawa). The method we used for evaluating the success of a prediction test is thus robust with regard to the algorithm and type of data used. Computational restraints prevented applying maximum-likelihood algorithms to our entire data set at once, so we used multiple overlapping subsets of sequences to perform these analyses. The data set was also too large for standard bootstrap analysis, so we estimated bootstrap values by using 10,000 PAUP FastStep bootstrap replicates. This number was determined by increasing the number of replicates until we obtained a consistent set of bootstrap values.
8. I. A. Wilson and N. J. Cox, *Annu. Rev. Immunol.* **8**, 737 (1990); D. C. Wiley, I. A. Wilson, J. J. Skehel, *Nature* **289**, 373 (1981).
9. Supplementary tables showing the codons used in alternative prediction tests are available at www.sciencemag.org/feature/data/1044188.shl
10. C. A. Bender and N. J. Cox, unpublished data.
11. N. J. Cox and C. A. Bender, *Semin. Virol.* **6**, 359 (1995).
12. W. Weis *et al., Nature* **333**, 426 (1988).

13. Supported in part by funds provided by the University of California for the conduct of discretionary research by Los Alamos National Laboratory, conducted under the auspices of the US Department of Energy. We gratefully acknowledge the technical expertise of H. Jing and the critical comments of S. Frank.

3 August 1999; accepted 3 November 1999

Complex Shear Wave Velocity Structure Imaged Beneath Africa and Iceland

Jeroen Ritsema,[1]* Hendrik Jan van Heijst,[1] John H. Woodhouse[2]

A model of three-dimensional shear wave velocity variations in the mantle reveals a tilted low velocity anomaly extending from the core-mantle boundary (CMB) region beneath the southeastern Atlantic Ocean into the upper mantle beneath eastern Africa. This anomaly suggests that Cenozoic flood basalt volcanism in the Afar region and active rifting beneath the East African Rift is linked to an extensive thermal anomaly at the CMB more than 45 degrees away. In contrast, a low velocity anomaly beneath Iceland is confined to the upper mantle.

Tomographic models of three-dimensional seismic velocity variations continue to improve our understanding of the structure of flow in Earth's mantle (*1*–*6*). It has long been recognized that higher than average seismic velocities are present in regions of the mantle with long-term subduction (such as the circum-Pacific region and Asia) and that lower than average velocity structures are present in the deep mantle beneath Africa and the Pacific Ocean where subduction has not occurred since the Jurassic. The interpretation of high velocity anomalies as subducting slabs of relatively cold oceanic lithosphere has gained support from recent tomographic models, which show tabular structures of faster than average velocity beneath several subduction zones (*7*, *8*) (Web figure 1). The complex shape and broadening of these slab-like structures may be a manifestation of the complex subduction zone process, large-scale plate motions, and the resistance to flow caused by the spinel-to-perovskite phase transition at 670 km depth (*9*). Although laboratory experiments (*10*, *11*) and computer models (*12*, *13*) demonstrate that hot upwellings may ascend into the mantle in a similarly complex manner, it is difficult to image narrow conduits of rapidly rising mantle plumes (*14*) in the deep mantle. In addition, tomographic models have not fully constrained the dimensions and shape of the large-scale upwellings beneath Africa and the Pacific Ocean (Fig. 1).

We studied the structure of upwellings in the mantle using seismic tomographic model S20RTS (*15*). We focused on the large-scale low velocity anomaly in the deep mantle beneath Africa, which was imaged in earlier tomographic models (*1*, *2*) (Fig. 1) and has been linked to surface manifestations of hot spots around Africa (*16*), the high elevation of southern Africa (*17*), and the ultra-low velocity anomalies at the base of the mantle beneath Africa (*18*). We compared this anomaly with the low velocity structure beneath Iceland. S20RTS is a degree-20 shear wave velocity model that incorporates surface wave phase velocities, body wave travel times, and free-oscillation splitting measurements (Table 1). These data cover the entire

[1]Seismological Laboratory, California Institute of Technology, Pasadena, CA 91125, USA. [2]Department of Earth Sciences, Oxford University, Oxford OX1 3PR, UK.

*To whom correspondence should be addressed. E-mail: jeroen@gps.caltech.edu

spectrum of seismic frequencies and, hence, constrain the long-wavelength and the short-wavelength seismic velocity variations.

We obtained phase velocity and travel time data high from digital global and regional network recordings (IRIS, GEOSCOPE, MedNet, CNSN, and PASSCAL) of moderate-size (magnitude, $M_w > 5$) earthquakes that occurred between 1980 and 1998. The surface wave data set contains over a million phase velocity measurements (on average 10 measurements per seismogram) of fundamental and higher mode Rayleigh waves with seismic periods ranging from 40 s to 250 s. Higher mode (up to the fourth overtone) phase velocity measurements, which constrain seismic structures in and below the upper mantle transition zone (400 to 1000 km depth), constitute a unique subset of these data (*19*). The body wave data set includes about 50,000 hand-picked absolute travel time measurements for a large variety of seismic phases that propagate through the lower mantle, including *S*, S_{diff} multiple surface reflections (*SS* and *SSS*), core reflections (*ScS*, ScS_2, and ScS_3), and core-phases (*SKS* and *SKKS*) (*20*). These phases provide a uniform sampling of the mid and lower mantle in the Northern and Southern hemispheres. The third type of data used were normal mode structure coefficients for multiplets below 3 mHz. These data are particularly useful to constrain the very long-wavelength (>2000 km) pattern of seismic velocity variation. It has been demonstrated that these data are a valuable addition to body wave and surface wave data to constrain velocity structures in the mid-mantle (*21*). We invert the entire data set for a model of shear velocity perturbation with respect to the Preliminary Reference Earth Model (PREM) (*22*) using an exact least-squares inversion technique (*23*).

Horizontal cross sections through model S20RTS illustrate that the low shear wave velocity anomaly beneath Africa has a complex three-dimensional shape (Fig. 2A). The African anomaly covers an extensive region in the lowermost mantle (4000 × 2000 km^2 at the CMB) beneath the southeastern Atlantic Ocean and it is connected to patches of relatively low velocity beneath central Africa, northwestern Africa, and the southern Indian Ocean. Structures with relatively high velocity anomalies beneath North and South America, the polar regions, eastern Asia and the Indian Ocean surround the African anomaly. The African anomaly is narrower at mid-mantle depths (2350 to 1100 km) and it is centered progressively further to the east and northeast with increasing height above the CMB. Vertical cross sections further illus-

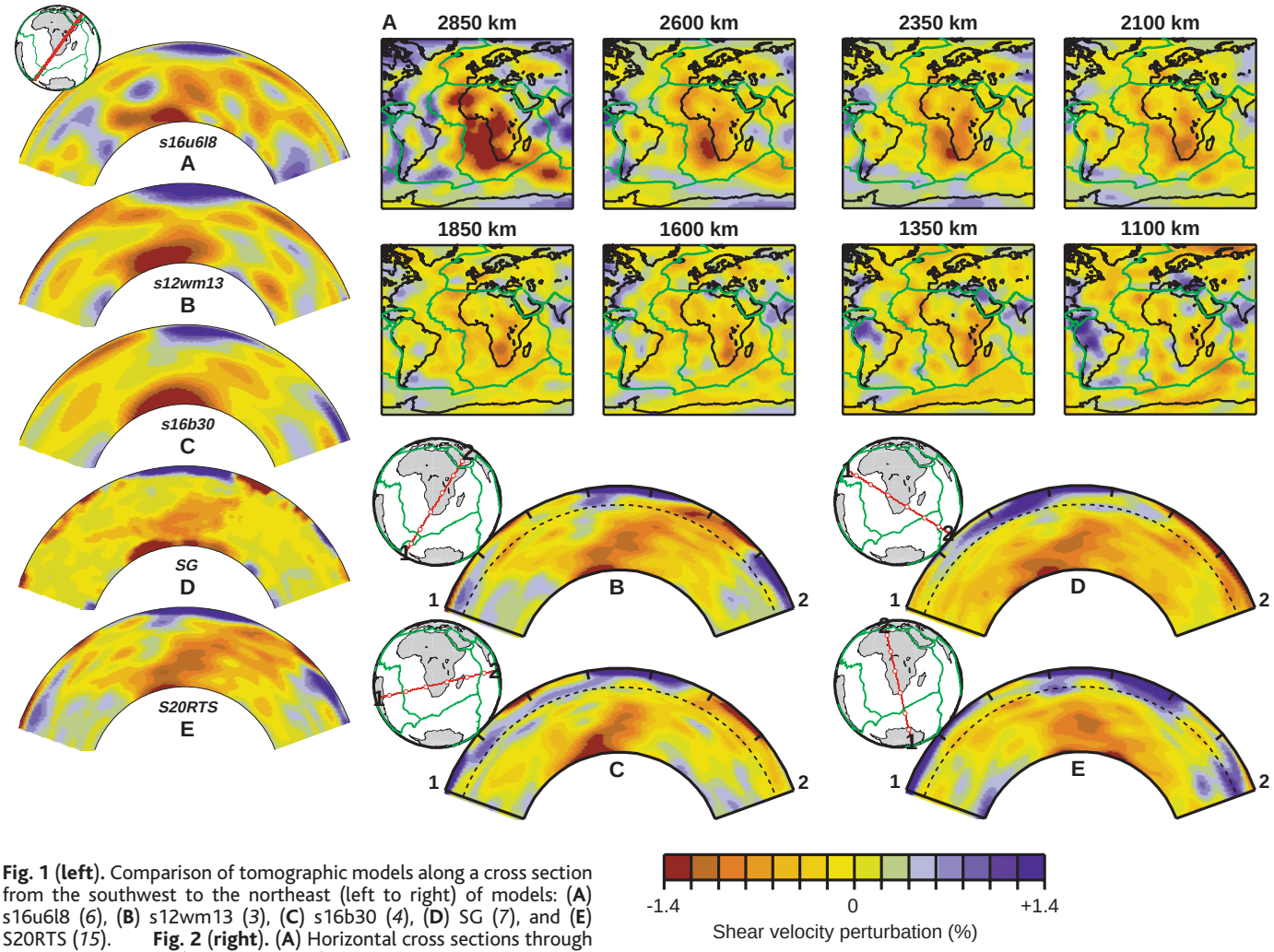

Fig. 1 (left). Comparison of tomographic models along a cross section from the southwest to the northeast (left to right) of models: (**A**) s16u6l8 (*6*), (**B**) s12wm13 (*3*), (**C**) s16b30 (*4*), (**D**) SG (*7*), and (**E**) S20RTS (*15*). **Fig. 2 (right).** (**A**) Horizontal cross sections through S20RTS at the CMB (2890 km depth), and at depths of 2600, 2350, 2100, 1850, 1600, 1350, and 1100 km. Relatively high velocity and low velocity regions are indicated by blue and red colors, respectively, with an intensity that is proportional to the percentage amplitude of the velocity perturbations compared with shear wave velocities from the PREM at these depths. Green lines represent plate boundaries and black lines outline land masses. (**B** to **E**) Cross sections along 140° wide great circle arcs. The dashed line represents the 670-km seismic discontinuity. Superposed are maps showing corresponding great circle arcs along which the cross sections are made. White circles on the great circle arc are plotted at 20° intervals and correspond to the bold tick marks shown in the cross sections. The color scale bar indicates the percent that the shear wave velocities are higher (positive percentages) or lower (negative percentages) than the PREM.

trate the continuity of the African anomaly at least 2000 km into the mantle (Fig. 2, B through D). Figure 2B shows that the African anomaly extends from the CMB beneath southern Africa into the upper mantle beneath the East African rift, while the tilt of the African anomaly toward the east and northeast is also obvious in the cross section of Fig. 2, C and D. This tilt may be enhanced by a lateral offset at a depth of about 2000 km in our model.

Model S20RTS indicates that the low velocity anomaly beneath Iceland is smaller in volume than the African anomaly (Fig. 3). The 660-km phase transition marks a lower boundary of the low velocity anomaly beneath Iceland (with up to 2.5% lower shear wave velocities compared to PREM velocities at this depth). The low velocity anomaly in the transition zone beneath Iceland may explain the change in the depth of the 410-km and 660-km phase transitions versus the predicted transition depths from PREM and mineral physics studies (*24*). However, a connection to the CMB by a narrow plume conduit, as recently suggested using *P* wave travel time tomography (*25*), is not modeled in S20RTS.

The finite extent of Backus-Gilbert resolution kernels (*26*) (Fig. 4 and Web figure 2) for three locations in the mantle beneath Africa indicates that small-scale volumetric heterogeneity (<500 km) is not resolved and that velocity contrasts are underestimated in S20RTS. However, shear wave velocity anomalies at points X, Y, and Z were independently derived because Backus-Gilbert kernels, determined for these points, do not overlap. Hence, the continuity of the low velocity anomaly and its tilt beneath Africa are not caused by preferential southwest to northeast body wave sampling.

A large-scale thermal upwelling (or an assemblage of several boundary layer instabilities) from the CMB is a consistent interpretation of the African anomaly. Although the images of the African anomaly cannot completely constrain the significance of compositional heterogeneity in the mantle (*27*) or the evolution of such an upwelling (*28*), they do indicate that the shape of the upwelling at its base is complex and that the upwelling does not ascend vertically

Table 1. Seismic data used in S20RTS.

Mode or phase	Number
Rayleigh wave phase velocities (T=40 to 275 *s*)	
Fundamental mode	1,367,712
First higher mode	169,600
Second higher mode	140,945
Third higher mode	125,341
Fourth higher mode	168,524
Body wave travel times	
S/S_{diff}	18,202
SS + *SSS* + *SSSS*	17,139
ScS + ScS_2 + ScS_3	5,172
SKS + *SKKS*	7,214
Normal mode splitting measurements	
$_0$S through $_8$S	2,036

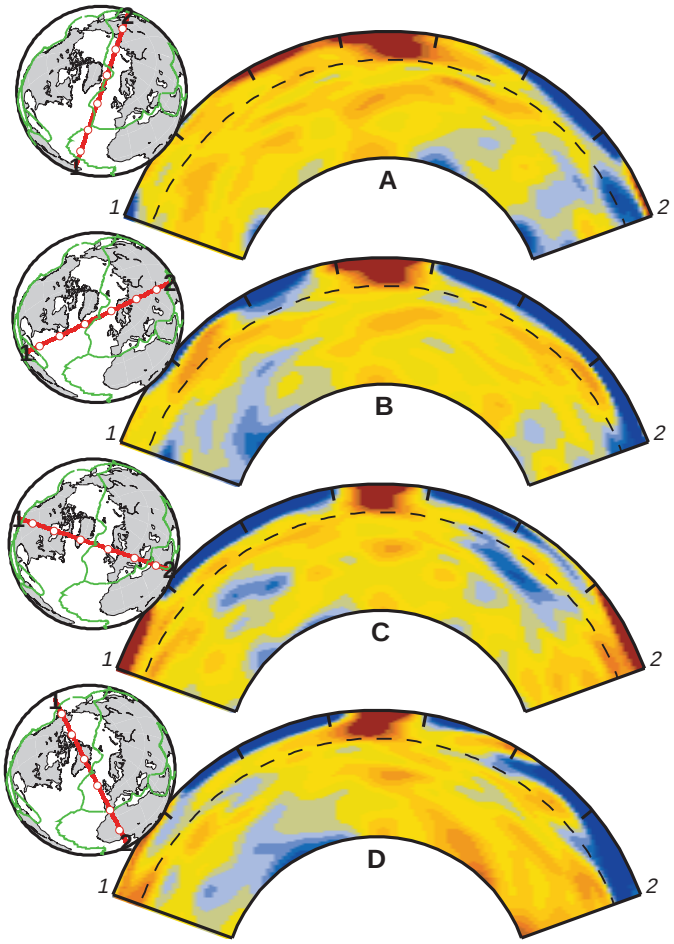

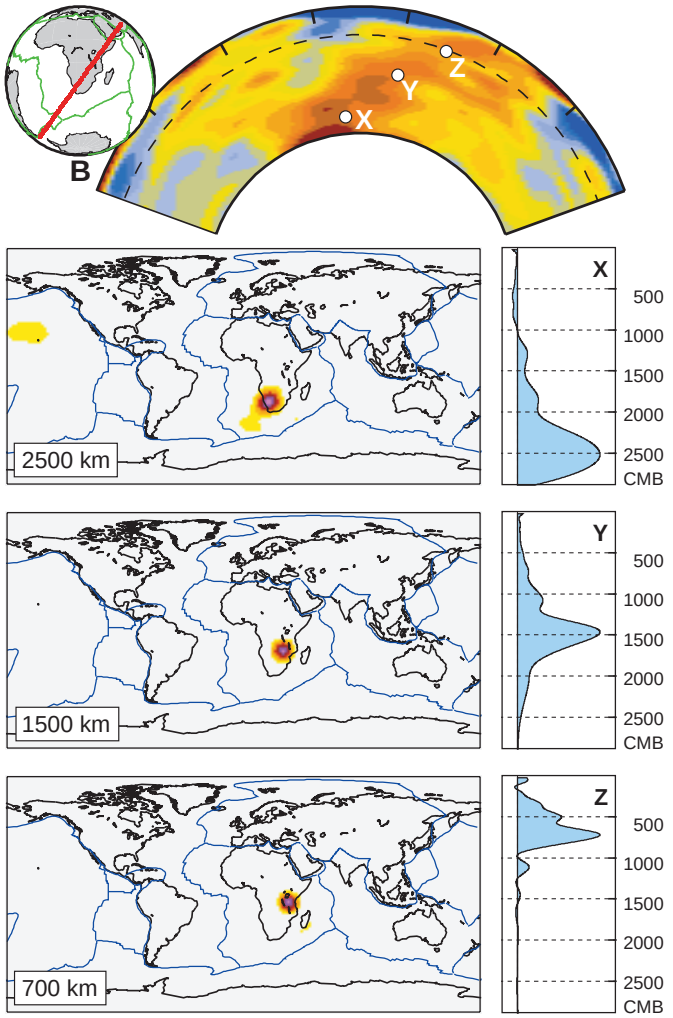

Fig. 3 (left). (**A** to **D**) Vertical cross sections through Iceland plotted with the same color scale and labeling as used in Fig. 2. **Fig. 4 (right).** Backus-Gilbert resolution kernels for locations X, Y, and Z at 2500, 1500, and 700 km depth, respectively, in the mantle beneath Africa. Horizontal cross sections through the Backus-Gilbert kernels are shown on the left. The relative amplitude of the kernels (from 0.1 to 1.0) is represented by nine colors, which range from yellow to red to pink. Regions where the Backus-Gilbert kernels have a relative amplitude lower than 0.1 are not shaded. The radial dependence of the kernels is shown on the right.

into the mantle. The shear of the upwelling may be a consequence of the migration of the African plate to the northeast since the breakup of Gondwanaland, interaction with mid-mantle heterogeneity, the 670-km phase transition or a putative physical boundary near 2000 km depth (*3*, *29*).

The weakening of the low velocity anomaly between 670 and 1000 km depth indicates that the upwelling is obstructed. Eventually, however, an upwelling may form in the transition zone beneath eastern Africa, which propagates along the base of the lithosphere into the East African rift region. The central location of the upwelling in the deep mantle beneath southern Africa can explain the anomalously high elevation of southern Africa and of its contiguous ocean basins and the high long-wavelength geoid over Africa and the Atlantic Ocean (*17*). The continuity of this upwelling into the upper mantle region beneath East Africa compels a link between a relatively hot CMB region and flood basalt volcanism that formed the Ethiopian traps and contributed to the rifting in the Red Sea, the Gulf of Aden, and along the East African Rift (*30*).

References and Notes

1. A. M. Dziewonski, *J. Geophys. Res.* **89**, 5929 (1984).
2. J. H. Woodhouse and A. M. Dziewonski, *J. Geophys. Res.* **89**, 5953 (1984).
3. W.-S. Su, R. L. Woodward, A. M. Dziewonski, *J. Geophys. Res.* **99**, 6945 (1994).
4. G. Masters, S. Johnson, G. Laske, H. Bolton, *Philos. Trans. R. Soc. London A.* **354**, 1385 (1996).
5. X.-D. Li and B. Romanowicz, *J. Geophys. Res.* **101**, 22,245 (1996).
6. X.-F. Liu and A. M. Dziewonski, in *The Core-Mantle Boundary Region*, M. Gurnis, M. E. Wysession, E. Knittle, B. A. Buffet, Eds. (American Geophysical Union, Washington, DC, 1998), pp. 21-36.
7. S. P. Grand, R. D. Van der Hilst, S. Widiyantoro, *Geol. Soc. Am. Today* **7**, 1 (1997).
8. H. Bijwaard, W. Spakman, E. R. Engdahl, *J. Geophys. Res.* **103**, 30,055 (1998).
9. Reviews of the fate of subducting slabs are given in P. Silver, R. W. Carlson, P. Olson, *Annu. Rev. Earth Planet. Sci.* **16**, 477 (1988), and T. Lay, *Annu. Rev. Earth Planet. Sci.* **22**, 33 (1994).
10. D. Bercovici and J. Mahoney, *Science* **26**, 1367 (1994).
11. C. Kincaid, G. Ito, C. Gable, *Nature* **376**, 758 (1995).
12. T. Nakakuki, H. Sato, H. Fujimoto, *Earth Planet. Sci. Lett.* **121**, 369 (1994).
13. D. A. Yuen, L. Cserepes, B. A. Schroeder, *Earth Planets Space* **50**, 1035 (1998).
14. H.-C. Nataf and J. C. VanDecar, *Nature* **364**, 115 (1993).
15. H. J. Van Heijst, J. Ritsema, J. H. Woodhouse, *Eos* (spring suppl.) **80**, S221 (1999).
16. W. J. Morgan, *Nature* **230**, 42 (1971); M. A. Richards, B. H. Hager, N. H. Sleep, *J. Geophys. Res.* **93**, 7690 (1988); C. J. Ebinger and N. H. Sleep, *Nature* **395**, 788 (1998).
17. B. H. Hager *et al.*, *Nature* **313**, 541 (1985); A. A. Nyblade and S. W. Robinson, *Geophys. Res. Lett.* **21**, 765 (1994); C. Lithgow-Bertelloni and P. G. Silver, *Nature* **395**, 269 (1998).
18. T. Lay, Q. Williams, E. J. Garnero, *Nature* **392**, 461 (1998).
19. Phase velocity of fundamental mode and up to the fourth overtone Rayleigh waves are determined using the Mode Branch stripping technique [H. J. Van Heijst and J. H. Woodhouse, *Geophys. J. Int.* **131**, 209 (1997)], involving cross-correlation of single-mode branch synthetics with long-period seismograms. Phase velocity maps of these fundamental and overtone Rayleigh wave data are presented in H. J. Van Heijst and J. H. Woodhouse [*Geophys. J. Int.* **137**, 601 (1999)].
20. Travel times are estimated by cross-correlating observed waveforms with normal mode synthetics, computed for the PREM (22) and Harvard Centroid Moment Tensor source parameters [A. M. Dziewonski, T.-A. Chou, J. H. Woodhouse, *J. Geophys. Res.* **86**, 2825 (1981)]. The waveforms are low-pass filtered at periods >15 s to reduce the effects of complex earthquake rupture processes and to increase signal-to-noise ratio. The exact waveform synthesis by normal mode summation facilitates the analysis of seismic phases with emergent onsets (for example, *SS*, *SKKS*, and S_{diff}) and small-amplitude phases (for example, *SSS* and ScS_2) recorded after the high-amplitude first arrivals.
21. The normal mode data used in this report are compiled by J. S. Resovsky and M. H. Ritzwoller [*J. Geophys. Res.* **104**, 993 (1999)] and have been retrieved from http://tagg.colorado.edu/geophysics/nm./dir/ of the University of Colorado.
22. A. M. Dziewonski and D. L. Anderson, *Phys. Earth Plan. Inter.* **25**, 297 (1981).
23. We account for the effects of topography and crustal thickness variation using the model CRUST5.1 [W. D. Mooney, G. Laske, G. Masters, *J. Geophys. Res.* **103**, 727 (1998)]. Seismic velocity variations are parameterized using 21 vertical spline functions and spherical harmonics up to degree 20. The inversion involves two steps: earthquake source relocation, and damped least-squares inversion for shear velocity structure. We iterate upon these steps until maximum variance reduction is obtained. The damped least-squares inversion for model parameters involves the computation of the eigenvalue decomposition, allowing us to determine model resolution. We do not apply smoothness constraints to the model.
24. Y. Shen, S. C. Solomon, I. Th. Bjarnason, C. J. Wolfe, *Nature* **395**, 62 (1998).
25. H. Bijwaard and W. Spakman, *Earth Planet Sci. Lett.* **166**, 121 (1999).
26. G. E. Backus and J. F. Gilbert, *Geophys. J. R. Astron. Soc.* **16**, 169 (1968). A Backus-Gilbert kernel $R(\mathbf{r}_0, \mathbf{r})$ describes how the shear wave velocity $V_s^m(\mathbf{r}_0)$ in the model at $\mathbf{r}_0$ is a spatial average of shear wave velocity in the actual Earth: $V_s^m(\mathbf{r}_0) = \int_V R(\mathbf{r}_0, \mathbf{r}) V_s(\mathbf{r}) d\mathbf{r}$. If resolution is perfect, Backus-Gilbert kernels are delta-functions $\delta(\mathbf{r}_0 - \mathbf{r})$. However, they are typically less localized due to the finite number of model parameters, limited data coverage, and model norm damping.
27. U. Christensen, *Ann. Geophys.* **2**, 311 (1984); P. J. Tackley, in *The Core-Mantle Boundary Region*, M. Gurnis, M. E. Wysession, E. Knittle, B. A. Buffet, Eds. (American Geophysical Union, Washington, DC, 1998), pp. 231–253; M. Ishii and J. Tromp, *Science* **285**, 1231 (1999).
28. S. Zhong and M. Gurnis, *J. Geophys. Res.* **98**, 12,219 (1993).
29. L. H. Kellogg, B. H. Hager, R. D. Van der Hilst, *Science* **283**, 1881 (1999).
30. C. Hofmann *et al.*, *Nature* **389**, 838 (1997); I. Manighetti *et al.*, *J. Geophys. Res.* **102**, 2681 (1997); C. Prodehl *et al. Tectonophysics* **278**, 121 (1997); C. J. Ebinger and N. H. Sleep, *Nature* **395**, 788 (1998); V. Courtillot *et al.*, *Earth Planet. Sci. Lett.* **166**, 177 (1999).

31. Data were provided by the IRIS and GEOSCOPE data management centers. This research was funded by a grant from the National Science Foundation. We thank D. Anderson, Y. Fialko, and M. Gurnis for helpful discussions. This is contribution number 8687 of the Division of Geological and Planetary Sciences at California Institute of Technology.

23 August 1999; accepted 9 November 1999

A Lower Mantle Source for Central European Volcanism

Saskia Goes,*† Wim Spakman, Harmen Bijwaard

Cenozoic rifting and volcanism in Europe have been associated with either passive or active mantle upwellings. Tomographic images show a low velocity structure between 660- and 2000-kilometer depth, which we propose to represent a lower mantle upwelling under central Europe that may feed smaller upper-mantle plumes. The position of the rift zones in the foreland of the Alpine belts and the relatively weak volcanism compared to other regions with plume-associated volcanism are probably the result of the past and present subduction under southern Europe.

The processes responsible for the formation of the Cenozoic system of rifts in central and western Europe are enigmatic. The rifts form an almost continuous system of extensional structures (Fig. 1) starting in the Valencia Trough [and possibly even further south in north Africa (*1*)], continuing through the Gulf of Lion and the Saône, Limagne, and Bresse grabens in France and the Rhine and Leine grabens in Germany and then bifurcating west into the Lower Rhine Embayment in the Netherlands and east into the Eger graben in the Bohemian Massif and into Poland.

Extensional activity along the European rift system started in the Eocene more or less contemporaneous with the main and late orogenic phases in the Alps in a belt around the Alpine collision front (*1*). Rifting was accompanied by localized volcanism and uplift possibly due to thermal doming. In several regions of the rift system, minor phases of older, pre-rifting volcanism have been dated (*2*). Seismicity defines zones of active extension in the Rhenish Massif, the lower Rhine Embayment, and the Massif Central (*3*). Active uplift (*1*, *4*) and volcanism only a few thousands years old (*2*) are documented in the Rhenish Massif, Massif Central, and parts of the Bohemian Massif. In

Vening Meinesz Research School of Geodynamics, Utrecht University, Post Office Box 80.021, 3508 TA Utrecht, Netherlands.

*To whom correspondence should be addressed. E-mail: saskia@tomo.ig.erdw.ethz.ch

†Present address: Institut für Geophysik, ETH Hönggerberg, 8093 Zurich, Switzerland.